3

Fine Grained Alumina-Based Ceramics Produced Using Magnetic Pulsed Compaction

V. V. Ivanov, A. S. Kaygorodov, V. R. Khrustov* and S. N. Paranin
Institute of Electrophysics UD RAS
Russian Federation

1. Introduction

Despite the numerous studies dedicated to the alumina fabrication and its properties research there is still an interest for this material. The main reason for this is the low cost of alumina and wide range of such unique properties as mechanical, electrophysical, thermal and chemical ones. High alumina values are fully realized on monocrystal leucosapphire only. But monocrystal material (by known reasons) cannot be used widely. Cheaper polycrystalline alumina is characterized by low toughness, brittleness, weak thermal resistance and low wear resistance. The general opinion for the realization of the whole potential of alumina is the minimization of its grain size. This is what the researchers's efforts are directed to. The usage of standard approaches namely, standard two-staged technology including cold uniaxial compaction and thermal sintering appears to be a preferable one. Dopants are used for alumina sintering and grain growth processes control. At that the usage of nanopowders compacted up to high density can lead to a formation of fine structure.

The aim of the work is to fabricate alumina-based ceramics with high wear resistance. It is achieved by the usage of weakly aggregated nanopowders and by the application of magnetic-pulsed compaction as well as by the addition of titania, magnesia and zirconia.

2. Initial powders

In present work the nanopowders, obtained by pulsed methods of electrical explosion of wires (EEW) (Kotov, 2003) and laser evaporation (LE) of the ceramic targets with given content (Kotov et al., 2002) were used. The powders were synthesized in the laboratory of pulsed processes of the Institute of Electrophysics UB RAS. These methods allow to obtain weakly aggregated nanopowders due to pulsed material heating and evaporation regimes and the condensation process managing.

The principal of the EEW powders is the formation of the mixture of boiling metal drops because of heating after the explosion of the conductor under the action of the high dense current (10^4-10^6 A/mm^2). This conductor spreads rapidly into the surrounding media. The flying drops are oxidized in the oxygen containing atmosphere (usually argon and oxygen

* Corresponding Author

mixture). The as-formed oxide particles are carried from the explosive chamber to the devices of caching and separation of the powder (electro filters and cyclones) by the gas flow. Al_2O_3 particle image is given on figure 1 (a).

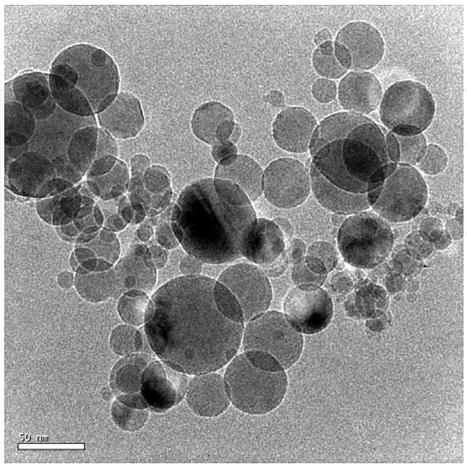

(a)

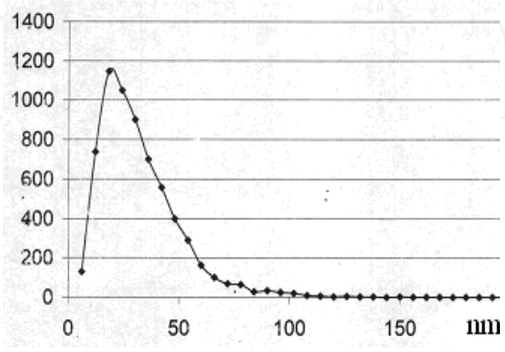

(b)

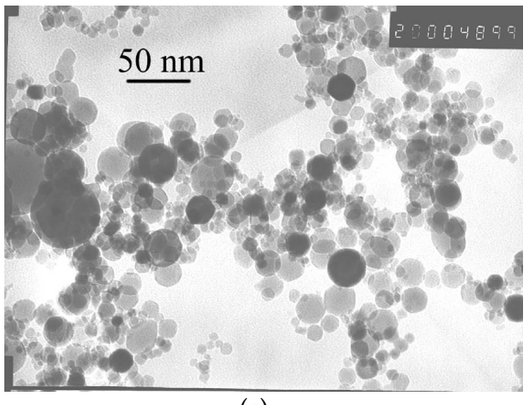

(c)

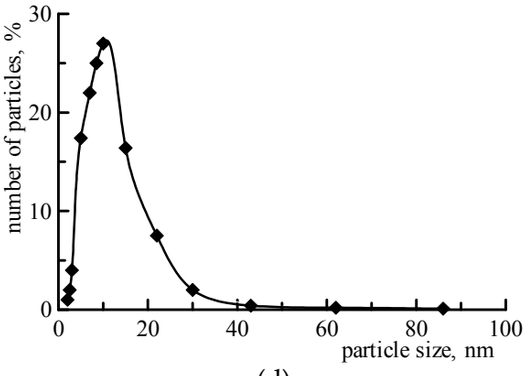

(d)

Fig. 1. The appearance of a nanoparticles made by: (a) - EEW process, Al_2O_3 and (c) - LE process, YSZ, with their size distribution (b) and (d), according TEM data.

Laser evaporation method (LE) is based on the usage of pulsed CO_2 laser to evaporate the ceramic target, prepared from micron-sized powders of the given chemical composition. The dispersion of the powders doesn't play any role here. The as-formed oxide particles are carried from the working chamber to the devices of caching and separation of the powder (electro filters and cyclones) by the gas flow (Ar, N_2 and O_2 mixture). For example, figure 1, (c) represents TEM image of the YSZ solid solution particles.

The disperse composition of the nanopowders was characterized by the average particle size of 20 - 30 nm (EEW) and 10 - 15 nm (LE) where the amount of particles that are larger than 0.2 microns was less than 8 wt. %. The nanopowders that were synthesized by pulsed EEW and LE methods are characterized mainly by the spherical-shaped particles and by the size dispersion with the positive asymmetry in the micron region (fig. 1 b and d). The distribution spectrum width of the particle sizes, obtained by LE method is 25% narrower

comparing to that of EEW method. Baring in mind that the particles are spherical and that they have relatively smooth surface, the objective characteristics of the powders is the average volume-surface diameter d_{BET} which is determined from the specific surface of the powder, S_{BET} (m^2/g):

$$d_{BET} = 6/\rho S_{BET}, \quad (1)$$

where ρ - density of the particle material in g/cm^3.

The peculiarity of this powders is their weak aggregation. The empirical criteria of weak aggregation (in present work) was the formation of the stable suspensions in alcohol (ethanol or isopropanol) under the ultra sonic action of 20 Watts/ml for 3-5 minutes.

In order to eliminate large (>200 nm) particles the powders were separated in alcohol. The mixing of different powders in order to obtain composites was performed here. The ultrasonic mixing during liquid evaporation provided the homogeneous distribution of the particles and prevented the formation of hard aggregates.

The general characteristics (phase composition, specific surface area, average particle size) that are used in present work are presented in tables 1 and 2.

№	Powder type	Phase content, wt.%	S_{BET}, m^2/g	dx, nm
1	Al_2O_3	0.2 γ + 0.8 δ	72	23
2	AM1	0.85 γ + 0.15 δ; Mg/Al = 1.5 at.%	69	24

Table 1. The characteristics of the initial powders, obtained by the explosion of the wire (EEW).

Al_2O_3 nanopowder was synthesized by EEW from pure alumina (table 1, p.1) (Kotov, 2003). In order to insert some dopants into alumina the composite compositions were prepared. A part of compositions was made by mixing of EEW and LE nanopowders (table 2, pp. 1 - 4), another part – by EEW alloy of the necessary content (table 1, p.2), and the third part – by the evaporation of the target from powder mixture (table 2 pp. 5, 6). TiO_2 and ZrO_2 doping was realized by the mixing of corresponding nanopowders: AT1 is the mixture of EEW nanopowders Al_2O_3 and TiO_2, AZ10 - EEW nanopowders Al_2O_3 and ZrO_2, A40, A85, - EEW nanopowder of Al_2O_3 and LE powder 2.8YSZ – solid solution of 2,8 mol.% of Y_2O_3 in zirconia (Kotov et al., 2002). Phase and disperse contents of the given composite nanopowders are the combination of the corresponding properties of its components. The homogeneity of particle distribution of both compositions in mixed composite nanopowders was provided by the ultra sonic action with continuous mixing during suspension drying.

The doping by MgO was realized on the stage of explosion of the Al-Mg alloy wire (table 1): AM1 nanopowder.

Two compositions were prepared by the ceramic target evaporation of the known content (table 2, A45 and A93 types) (Kotov, 2002).

The differences in the preparation regime are seen also in phase and granular content of nanopowders. AM1 nanopowder (table 1), obtained by EEC of Al-Mg alloy, on the contrary

from EEW of pure alumina, mainly consists from alumina γ-modification. As MgO dissolves in γ and δ-alumina modifications (Smothers & Reynolds, 1954), there were no Mg containing phases found in this powder. The differences in phase content of the EEW alumina and AM1 powders are demonstrated by the diffractograms (a) and (b) on figure 2.

A45 and A93 nanopowders (table 2), obtained by the ceramic target of given content are characterized by the complex phase content and smaller average X-ray size comparing to mixed powders of close content (A40 and A85). The peculiarities of their phase contents are illustrated by the X-ray diffractogramms (fig. 3, a and b).

№	Powder type	Composition,wt. %	Phase content, wt.%	Production method	S_{BET}, m^2/g	dx nm	dx_2 nm
1	AT1	99 (Al_2O_3) + 1 (TiO_2)	Al_2O_3: 0.20 γ + 0.80 δ TiO_2: 0.25 a + 0.75 r	EEW+ suspension mixing	56	22 - δ	48 - r 44 – a
2	A40	40 Al_2O_3 + 60 2.8YSZ	Al_2O_3: 0.20 γ + 0.80 YSZ: t	LE/EEW+ suspension mixing	73	24 - δ	17-t
3	A85	85 Al_2O_3 + 15 2.8YSZ					
4	AZ10	90 Al_2O_3 + 10 ZrO_2	Al_2O_3: 0.20 γ + 0.80 ZrO_2: 0.6 m+0.4 t	EEW+ suspension mixing	72	24 - γ	50 - m 28 - t
5	A45	45 Al_2O_3 + 55 1.6YSZ	18 γ+ 43 t + 39 c	LE of the ceramic target with the given content	81	13 - γ	10-t 8-c
6	A93	93 Al_2O_3 + 7 1.6YSZ	90 γ+1 t + 9 c		86	15 - γ	8-t 6-c

S_{BET} – specific surface area, dx – the average crystallite size of Al_2O_3 defined by the X-ray analysis, dx_2 – the average crystallite size of the additional phases, γ and δ - alumina phases, m, t and c – monoclinic, tetragonal, and cubic phases of ZrO_2(YSZ), a and r – TiO_2 modifications anatas and rutile.

Table 2. The characteristics of the composite nanopowders.

The notable diffusion background in the $2\Theta < 40°$ diffraction angles indicates the presence of sufficient fraction of amorphous alumina in LE nanopowders. Besides this the tetragonal modification of zirconia, as well as the cubic one, had the periods of the crystal lattice that were substantially smaller than that of the corresponding given yttria concentration. The same effect was seen on other Al_2O_3+YSZ composite powders earlier and it is connected with the dissolving of alumina in zirconia (Srdic´ et al., 2008). Knowing that ionic radius of aluminum is 20 % smaller that the radius of Zr and assuming the effect of elementary cell volume decrease to be linear at Zr atoms substitution by Al atoms, the content of alumina in each zicronia phase was estimated. In particular for A45 powder the alumina content was 0.9 and 23 mol.% in tetragonal and cubic zirconia modifications correspondingly. Thus the LE method leads to a formation of zirconia modifications containing a substantial amount of dissolved alumina along with yttria. The substantial amount of cubic phase at low concentration of yttria – 1.6 mol.% indicate on the stabilizing role of alumina dissolved. Small X-ray size of zirconia that are notable smaller than the particle size of the individual 2.8YSZ (table 2) could be connected with the influence of alumina dissolved.

Thus the absence of some Mg containing phases as well as the presence of Al_2O_3+ZrO_2 solid solution indicate the more uniform distribution of the components in AM1, A45 and A93 nanopowders.

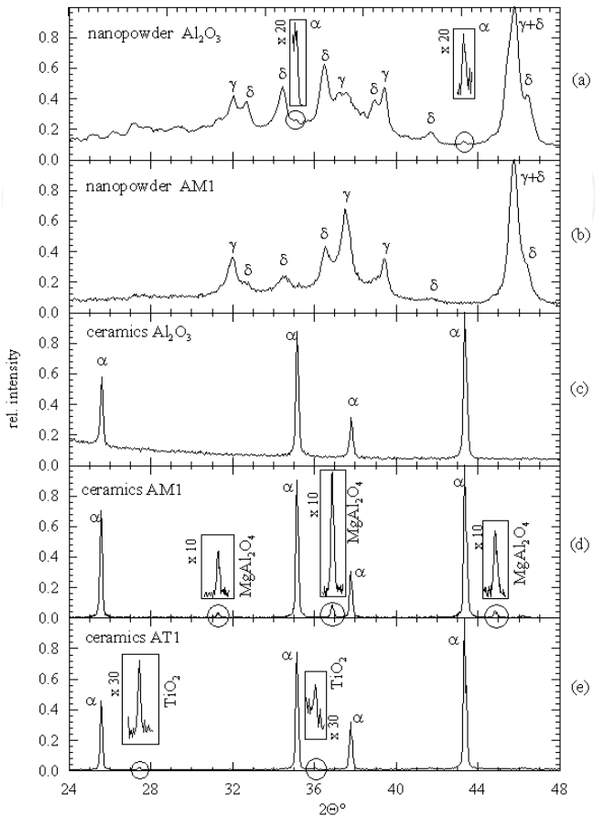

Fig. 2. XRD data (Cu Kα) for EEW nanopowders (a) - Al_2O_3, (b) - AM1 and sintered ceramics Al_2O_3 (c), AM1 (d), AT1 (e).

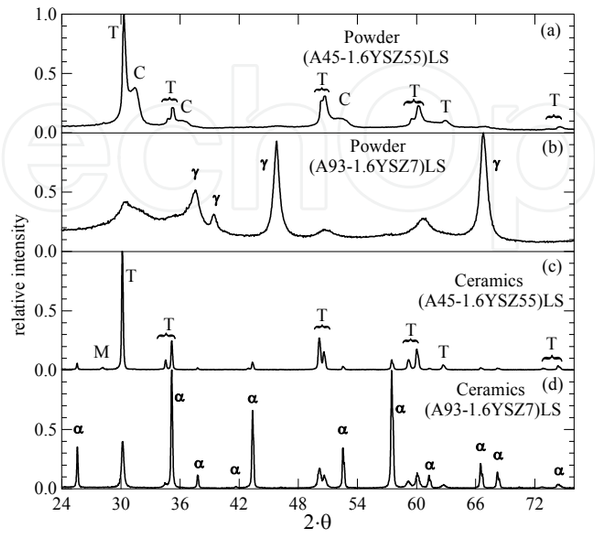

Fig. 3. XRD data (Cu Kα) for LE nanopowders (a, b) and sintered ceramics (c, d).

3. Experimental methods

3.1 MPC, the magnetic-pulsed compaction method

At nanosized particles the properties that prevent the consolidation of the particles into homogeneous compact material become sufficient: the specific bound energy as well as the amount of agents adsorbed and aggregating ability increases. That is why the nanosized powders are characterized with unsatisfactory compressibility and hence, the traditional static methods don't allow to reach high compacts density (Vassen & Stoever, 1992). This leads to a formation of large pores and rapid grain growth during sintering (Chen & Mayo, 1993). The nanopowder compaction and recrystallization difficulties upon sintering limited substantially the possibilities of the traditional compaction methods as well as sintering for fabrication of nanostructured materials and motivated for the searching of new approaches. For this class of nanomaterials hot isostatic pressing (HIP) method appeared to be the most perspective for the fabrication of high dense bulk zirconia ceramics with the grain size less than 50 nm (Hahn & Averback, 1992). Though from the point of view of shaped variety and cost decrease the traditional technology (cold pressing with the following sintering at normal pressure) is still the best one.

In order to fabricate dense compacts from nanosized powders the use of intensive pulsed compression methods appears to be quite attractive. The fast movement of the powder medium makes it possible to overcome the interparticle friction forces effectively. That is why high (> 0.6) relative densities can be achieved (Graham & Thadhani., 1993).

In present work the uniaxial magnetic-pulsed press (Institute of Electrophysics, Ekaterinburg, Russia) was used (Ivanov et al., 1999). It allows to produce pulsed pressure up to 1000 kN. The MPC method is based upon the principle of the throwing the conductor out of the pulsed magnetic field zone. The throwing force is the result of the interaction of the currents in the conductor and the magnetic field. In our research we've used well-known scheme of the conductor's acceleration (Fig. 4). The pulsed generator with the capacitive storages have been applied as the sources of the pulsed power currents and the magnetic fields. The capacity of energy, the voltage of the storage, and the characteristic pulse duration of the device figured on the scheme are 20 kJ, 5 kV, 120 - 360 μs.

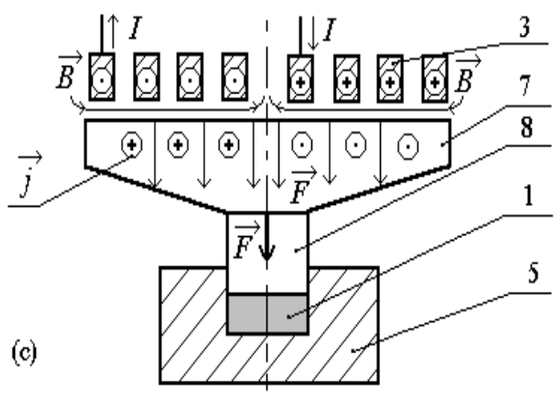

Fig. 4. Scheme of the pulsed magnetic compaction (MPC). 1- powder; 3- inductor; 5- mould; 7- concentrator; 8- piston.

The pulse of the pushing magnetic force on the side of the inductor 3 is apprehended by the hard current-conducting concentrator 7. The concentrator transmits the mechanical pulse to the piston 8 made of the hard-alloy which compresses the powder inside the mould. The high pulsed pressures in the mould (> 1 GPa) are achieved because of the fact that the area of the piston cross section is smaller than the area of the concentrator surface faced with the inductor.

By changing the pulsed pressure amplitude the compacts with relative density up to 0.7 were obtained. In present work the disk-shaped compacts 15-30 mm in diameter and 1.0-3.5 mm thick were used. It should be noted that the densities of the compacts from nanopowders achieved at least 10 - 15% higher than that of traditional "cold" static methods (Ivanov et al., 1997). The fracture image of the MP pressed alumina and YSZ nanopowders is shown on figure 5. The homogeneous location of grains with small amount of pores can be pointed out. The X-ray analysis indicate the intensive mechanical activation of the compacted powders. First of all, the additional peak widening appears. It is connected with the microdistortion of the crystalline lattice of about 0.1%. Second of all, the increase of the stable modifications is observed. For instance, in MP pressed weakly aggregated EEW alumina powder the notable amount (around 1-2 wt.%) of θ– and α– modifications appear in EEW alumina powder, doped with MgO (AM1) the amount of δ-alumina increases on 5 - 6 wt.%. At the same time the amount of less stable γ–alumina decreases (fig 2). The same effects were discovered earlier at EEW TiO_2 nanopowder compaction. Here the amount of more stable and dense rutile increased on about 7% at the decrease of the anatase amount (Ivanov et al., 1995). At that the specific area of the compacts decreases on 10 - 20% comparing to the initial powder. This fact indicated the sufficient increase of the interparticle contacts in the compacts. This leads to the increase of the starting sintering speed.

In general such changes promote the intensification of the following sintering process.

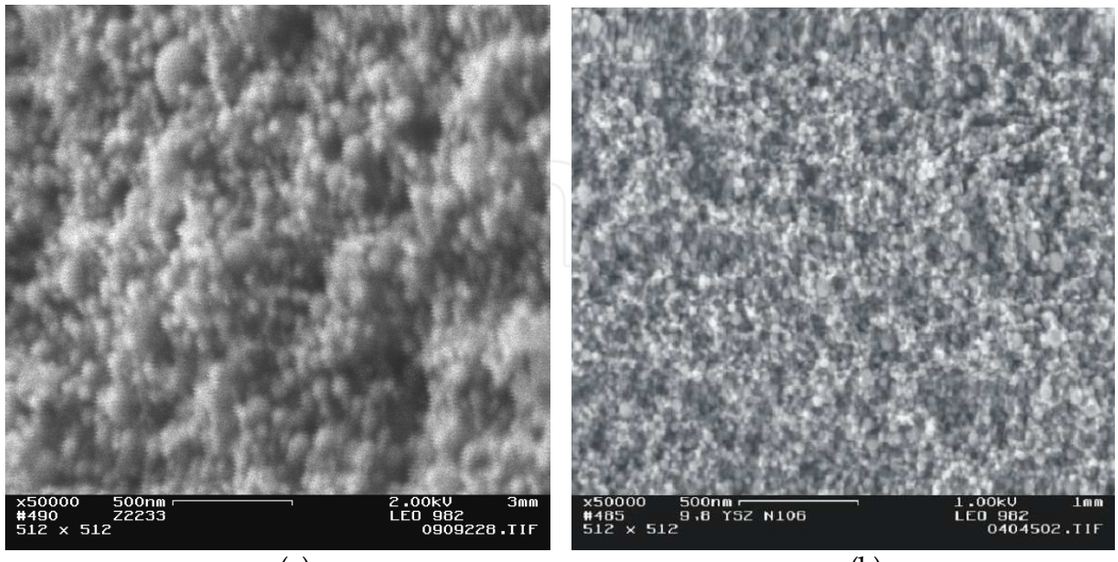

(a) (b)

Fig. 5. MPC green body fracture REM images of nanopowders (a) Al_2O_3, (b) YSZ.

3.2 Sintering and attestation methods

The shrinkage dynamics upon sintering was investigated at constant heating rate at the temperatures up to 1460°C in air by the dilatometric analysis using Netzsch DIL 402C. During sintering the quenching was used for the determination of phase content and grain size. X-ray diffraction method (Brucker D8 DISCOVER diffractometer, Cu Kα radiation) was used for phase content, CSR - coherent scattering region or the dimension of the crystal phases d_x determination in the initial powders, green bodies and ceramic samples. The d_x size was determined by the widening of the diffraction peaks using the Sherrer-Selyakov method. TEM (Jeol JEM 2100) was used for the nanopowders particles analysis. The structure of the ceramics fractures was studied via AFM (NT-MDT Solver P47) and REM (LEO982).

The density of the samples was determined by weighing in water, the specific surface area – by the adsorption of the N_2 or Ar (Micromeritics Tristar 3000).

Microhardness (Hv) and fracture toughness (K_{IC}) of the ceramics was determined by Vickers indentation method at 2 and 7 N load correspondingly (Micro Materials Ltd Nanotest 600).

The relative wear resistant was tested in water abrasive suspension of the aluminosilicate with the 5-50 microns particles as described in (Bragin et al., 2004).

4. Results and discussion

4.1 Sintering of nanopowders Al_2O_3 and influence of additives of MgO, TiO_2

Upon studying the alumina ceramics fabrication from the nanosized powders, containing polymorphs g and t, it appears to be actual to reveal the role of the multistep polymorph transition $\gamma + \delta \rightarrow \theta \rightarrow \alpha$. The influence degree on the whole sintering process is sufficient as the last stage is accompanied by the rapid grain growth of the appearing α - Al_2O_3 (Freim et. al., 1994). At that the features of the polymorph transition are essentially dependent from the quality of the initial powder (disperse and phase content, particles shape etc.) (Lange, 1984), density of its packaging [6] and the nature of the dopants that are inserted in alumina intentionally (Smoothers & Reynolds, 1954).

The influence of the dopants on the polymorph alumina transition upon nanopowders sintering, compacted up to high relative density (around 65%) is illustrated on figure 6. The addition of titania (fig. 6. a) decreases the temperature of the starting point of the polymorph transition relative to pure alumina, meaning the decrease of the temperature of the starting point of the shrinkage of the material (comparison a, b, and c on fig 6.). Moreover, the polymorph transition runs in this system at sufficiently lower densities, showing the decrease of the activation barrier comparing to pure alumina. In contrast to titania (fig. 6. a) magnesia increases the temperature border of the polymorph transition, increases its speed sharply and shrinkage speed in general (fig. 6. b).

Thus the form of the shrinkage curve of the compacts from the nanopowders of the metastable forms of alumina is determined by the processing of the polymorph transitions of alumina to stable α-Al_2O_3. At the staring stage ($t < T_A$) the material consists of the γ, δ, and θ phases mixture. The polymorph transition $(\gamma + \delta + \theta) \rightarrow \alpha$ starts at T_A temperature and can

be T_B considered as the temperature of the polymorph transition completion. At $t > T_B$ the material consists of α-alumina and at T_C the α–alumina shrinkage starts. Thus the shrinkage curve showed in fig. 7 is a sum of two S-shaped curves: the shrinkage curve defined by the polymorph transition starting at T_A and shrinkage curve upon sintering (the decrease of the porosity) staring at T_C. The T_A values of the polymorph transition are shown in table 3. The increase of T_A leads to the highest shrinkage speed in the T_A-T_B region of the AM1 nanopowder.

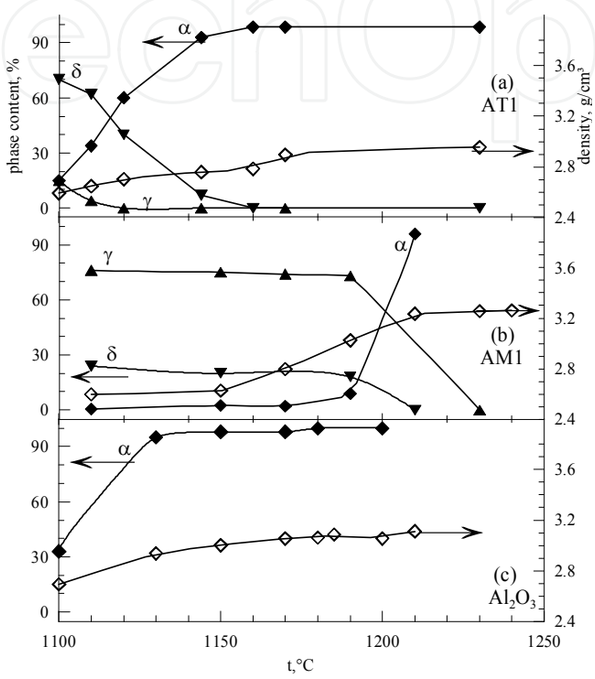

Fig. 6. Shrinking and γ, δ, α- Al_2O_3 concentration curves during alumina nanopowders sintering. Doping with: (a) - titania, AT1, (b) - magnesia, AM1, (c) - Al_2O_3 without dopants; constant heating rate 10°C/min.

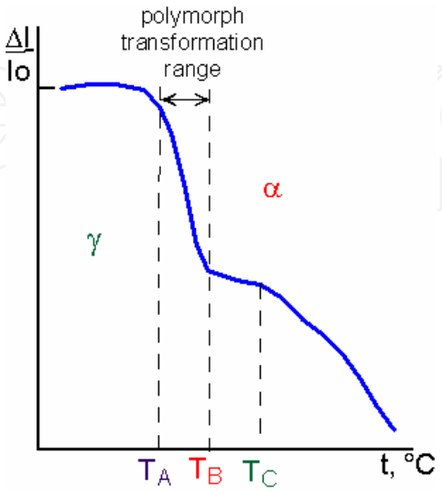

Fig. 7. Generalized sintering curve of alumina nanopowders.

Al_2O_3	AT1	AM1	A40	A85	A45	A93	t-YSZ
1050	1090	1140	1040	1170	1140	1150	850

Table 3. The temperatures T_A (±20°C) of the shrinkage beginning of nanopowders at constant heating rate 5°C/min.

The sufficient influence of the second phase nature on the grain structure evolution upon sintering of the ceramics is found (fig. 3.8). The size of the primary α–crystallites that are formed during sintering of the AM1 (MgO doped Al_2O_3) ceramics is comparable to the size of the crystallites of the initial metastable alumina modifications (fig. 3.8 b). The abnormal size change of the α-alumina crystallites in the system doped by TiO_2 is found (fig. 3.8 a). The size of the primary α–crystallites, as in the case of undoped alumina, is sufficiently larger than the size of the initial phases crystallites. Although in the temperature region of the mass formation of α–modification a large amount of the crystallites comparable with the crystallites of the initial modifications in terms of size appear. The following sintering is accompanied by a monotonic grain growth. The effect of the decelerated of the α–alumina crystallites upon magnesia doping (AM1, figure 3.8 b) is found. At equal densities the grain size of the alumina ceramics doped with titania (figure 3.8, a) is much larger comparing to AM1.

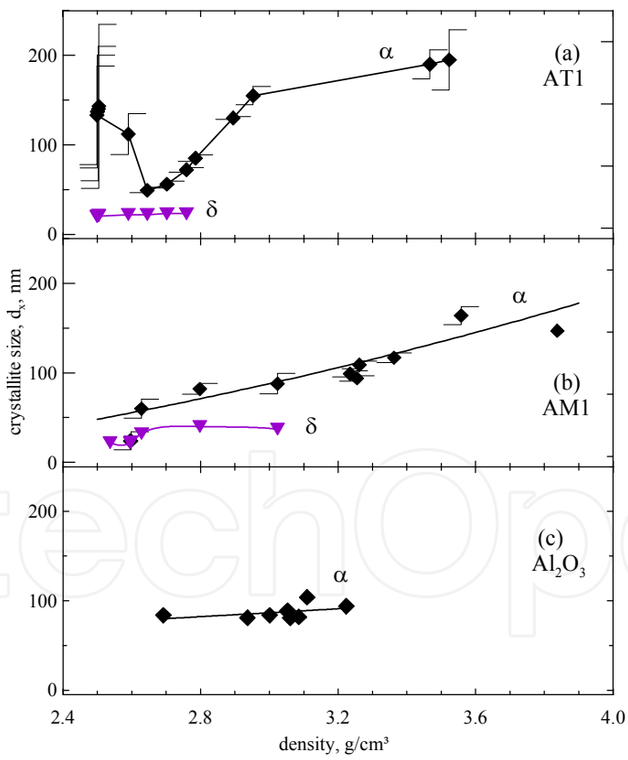

Fig. 8. Average X-ray crystallite size evolution upon sintering of the alumina ceramics, doped with: (a) - titania, AT1, (b) - magnesia, AM1, (c) - Al_2O_3 without dopants; constant heating rate 10°C/min.

At our opinion the positive role of the magnesia addition in fabrication of the dense and hard alumina-based ceramics is connected with the nature of the magnesia influence on the

diffusion processes upon alumina sintering, as well as with the technique of the additive insertion. It's important to note that MgO is dissolved in alumina nanopowder at atomic level and it doesn't form separate phases. The second $MgAl_2O_4$ spinel phase along with the α–alumina appears only during sintering of the AM1 compacts. It is seen from the comparison of the X-ray patterns of the initial powder (fig. 2, b) and sintered ceramics (fig. 2, d). On the contrary in AT1 ceramics there were no signs of mixed combination with alumina and titanium found. The α–alumina and TiO_2- rutile peaks are clearly seen on x-ray patterns (fig. 2, e).

The ceramics structure data, from analysis of the fracture images obtained by AFM in "height" and "Mag-cos" modes (figures 9 and 10) prove the X-ray data. In all cases the material consists of polycrystalline blocks, which shape and size depend on the dopant. The

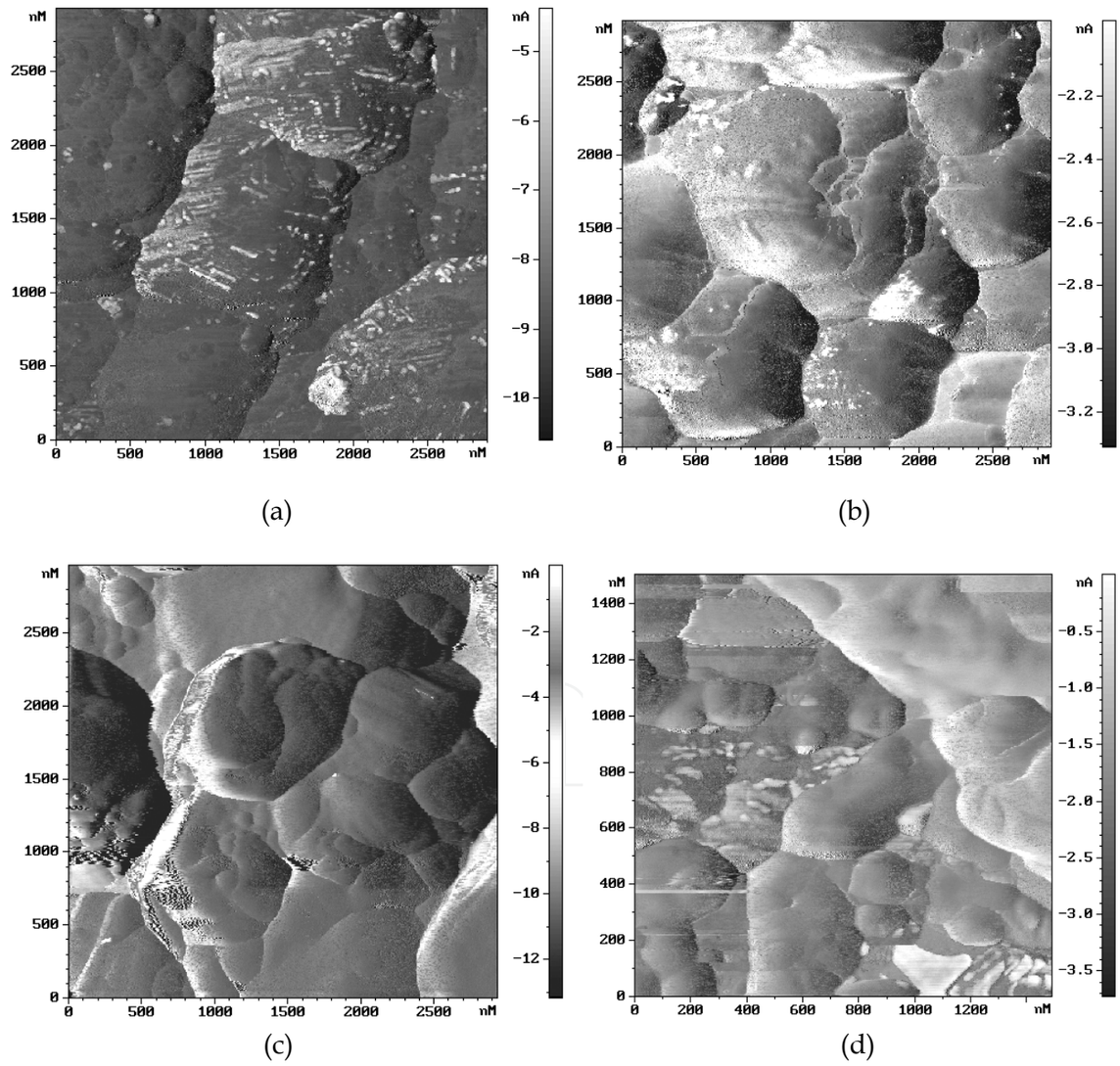

Fig. 9. Ceramic fracture AFM images of (a) - AM1 (τ_s = 6 min); (b) AM1 (τ_s = 30 мин); (c) AT1 (τ_s = 6 min); (d) AZ10 (τ_s = 60 min). ("Mag-cos" mode).

blocks's average size, d, given in table 4, and obtained by the intersection method of the AFM images clearly demonstrate the inhibitory influence of the MgO and ZrO_2 on the recrystallization processes in alumina matrix. It's worth mentioning the originality of MgO dopant which is uniformly dissolved in the initial metastable alumina and its segregation as $MgAl_2O_4$ nanocrystals on the boundaries of the matrix α–alumina crystals takes place at the polymorph transition to α-alumina only. On AFM images, taken in "Mag-cos" mode (fig. 3.9, a) the uniformly distributed contract light regions with around 20 nm in size are clearly seen.

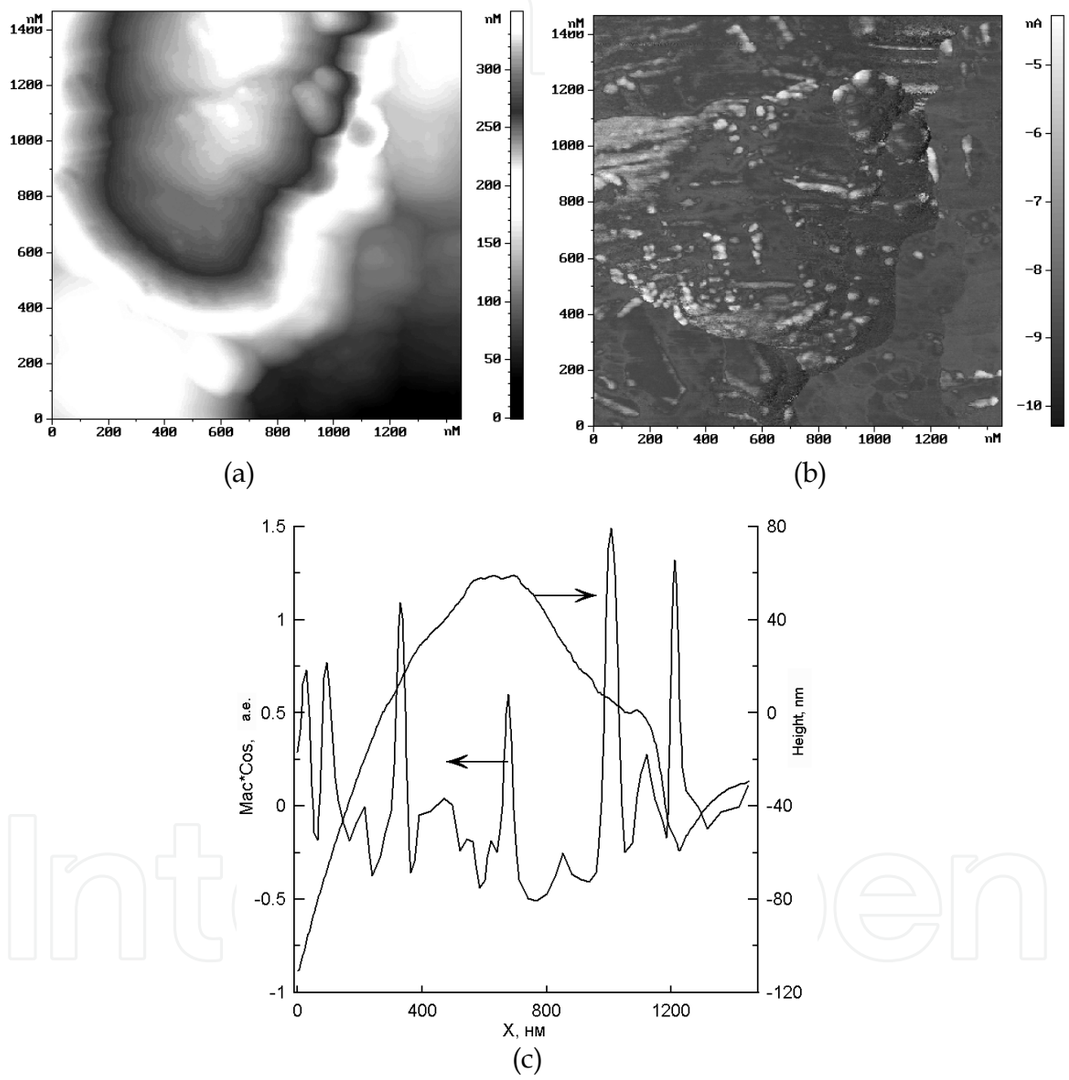

Fig. 10. AM1 ceramic fracture AFM images in (a) "height" and (b) "Mag-cos" modes with the corresponding profiles at Y=800 nm (c).

Probably these regions correspond to the second phase - $MgAl_2O_4$, defined by X-ray. It is proven by the combined structural analysis in "height" and "mag-cos" modes (figure 10). Clear peaks on the "mag-cos" curve (fig. 10, c) and corresponding smooth relief contour show the invariation of the block surface elastic properties and the presence of the doped

phase. This peculiarity is present upon the decrease of the sintering dwell time of such ceramics (fig. 9, b). Thus the doping by MgO allowed obtaining fine and homogeneous structure in alumina ceramics with uniformly dispersed $MgAl_2O_4$, nanophase over the grain surface leading to grain growth ingibition.

In case of the TiO_2-doped ceramics the largest blocks are observed (fig. 9). Its surface, in contrast to the mentioned above types of ceramics, is smooth. This fact doesn't allow to state the substantial difference between the crystal and block size. The accumulations of the doped phase are non-uniformly distributed over the volume. They are localized as about 100 nm thick interlayers between blocks (see light regions on fig. 9). Some isolated grained of the same size can be also seen.

4.2 Shrinkage peculiarities upon the sintering of the alumina nanopowders based ceramics doped with ZrO_2

A wide range of Al_2O_3+ZrO_2 compositions was studied (table 2). Pure zirconia as well as partially stabilized zirconia in tetragonal modification – as solid solution with Y_2O_3 (t-YSZ) with concentration of 1.6 and 2.8 mol% was used. The notable difference of the shrinkage curves of the nanopowders mixtures from the composite LE -nanopowders can be seen (fig. 11). It should be noted that LE nanopowders differ by sufficiently nonequilibrium material state, namely large fraction of alumina as solid solution in zirconia and in amorphous state. That is why its shrinkage behavior sufficiently differs from other nanopowders. It can be seen, that the shrinkage trend of the latter (A45 and A93 pp. 5 and 6 of table. 2) though the large difference of the Al_2O_3/t-YSZ ratio. On the other hand some differences of the nanopowders with close composition (A93 and A85) are seen. The shrinkage of the A85 nanopowder, obtained by the mechanical mixing of two powders (p.3 table 2), is similar to the shrinkage of the metastable alumina with the only difference in elevated for 100°C sintering temperature, as the shrinkage behavior of the A93 LE nanopowder is close to the shrinkage of t-YSZ, with 200°C temperature up shift (table 3).

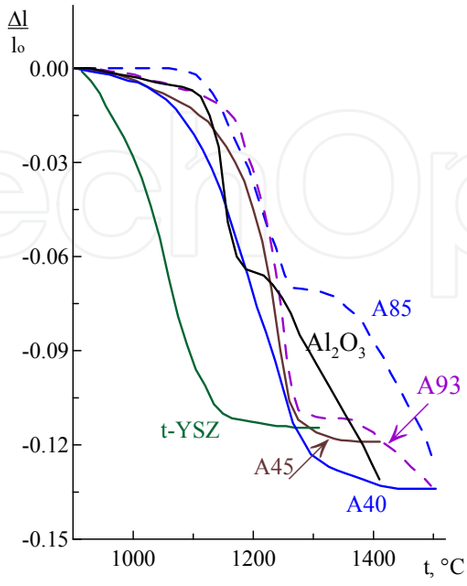

Fig. 11. Shrinking curves of nanopowders Al_2O_3 + t-YSZ (constant heating rate 5°C/min).

It is seen that the shrinkage curve of A40 and A45 compositions doesn't have the typical fracture, peculiar to the metastable alumina sintering. Bearing in mind the difference of the starting shrinkage temperatures of alumina and t-YSZ, it can be assumed that by the beginning of the $\gamma \rightarrow \alpha$ polymorph transition in alumina, the zirconia matrix is already formed. That is why the effect of the alumina crystal volume change is not notable on the shrinkage curve.

4.3 Peculiarities of the structural-phase state of the composite submicron alumina matrix ceramics with the YSZ and ZrO_2 additives

It appeared that in alumina exceeded ceramics the addition of zirconia doesn't lead to a substantial alumina grain growth inhibition effect upon sintering (fig 12). The average X-ray crystallite size of α-Al_2O_3 increases monotonously out of the confidence range of the X-ray method at 0.98 dense ceramics and denser. The nanopowders synthesis route appeared more important. It is seen on figure 12 that the crystallites size of α-Al_2O_3 in the ceramics, obtained from composite LE nanopowder (A93 type) is substantially larger than that of the ceramics, sintered from A85 nanopowder, obtained by the mixing of the individual nanopowders: EEW Al_2O_3 and LE 2.8YSZ.

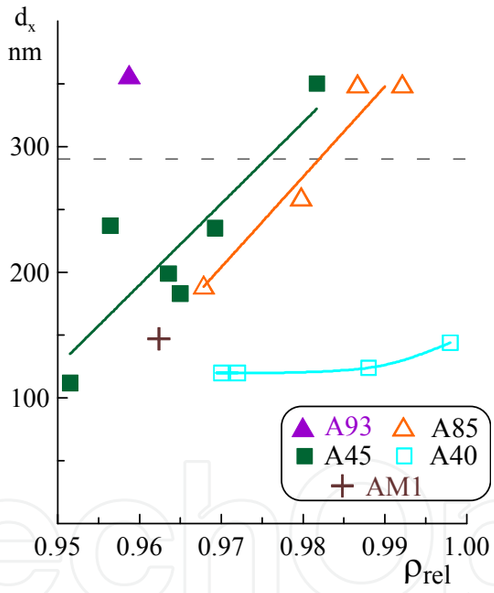

Fig. 12. Evolution of the average α-Al_2O_3 crystallite size during sintering of ceramics Al_2O_3 + t-YSZ. (constant heating rate 5°C/min) Dotted line shows the border of the confidence range of the X-ray method.

The notable effect of the grain growth limitation is obtained in the A40 ceramic samples where the volume fractions of Al_2O_3 and T-YSZ were approximately the same. While the density was reaching the theoretical limit the X-ray crystallite size didn't exceed 140 nm (fig 12 and table 4). In this case the limitary crystalline size can be limited by the homogeneity of the Al_2O_3 and T-YSZ initial powders mixing level reached. Perhaps the nanopowders mixing took place at aggregates level and the limitary crystal size in ceramics was determined by the quantity of the material in the volume of the single aggregate.

The visual interpretation of the X-ray peaks widening is given on figure 13 for the corundum doublet peak {024}. It is seen that the width of the reference peaks of coarse grained ceramics is the smallest one and two peaks are clearly separated. The corresponding peaks for the composite ceramics are merged together and are barely observable due to the presence of the shelf on the right side of the peak merged. At almost equal ceramics relative density (0.965) the peaks of the composite containing approximately equal volume fraction of tetragonal zirconia (2.8YSZ) and Al_2O_3 are the widest ones. This shows the finer structure of the ceramics with such composition.

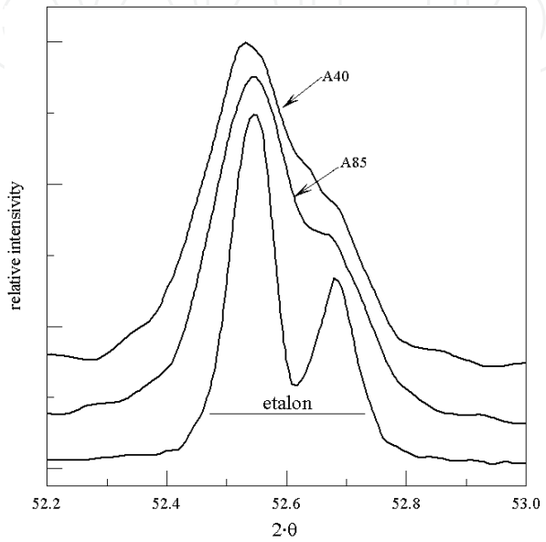

Fig. 13. X-ray corundum doublet reflex {024} (Cu K_α) for two composite ceramic Al_2O_3+YSZ, in comparison with rough crystalline ceramics Al_2O_3.

The second phase (Al_2O_3) didn't influence substantially on the grain growth of t-YSZ. While reaching the theoretical density the average X-ray crystallite size in all types of ceramics, including individual 2.8YSZ, becomes almost identical, around 70 - 90 nm.

Two consequent states of the polycrystalline structure at 0.92 and 0.97 densities are shown on the AFM images of the ceramics fractures (fig. 14). As the ceramics density increases (independently of the powder synthesis route) the general trend of the relief development is tracked. At relative density of 0.92 the relief consists of large blocks on the surface of which the boundaries of smaller grains are clearly seen (fig. 14, a and b). At relative density of 97% small fragments located on the surface of large blocks become less notable (fig. 14, c and d). The fraction of fractures that take place over the grain volume increases as the relief elements (formed upon crystal fracture) appear. There are practically no separated small particles in the bulk of the material. The "roundness" of the boundaries disappears. At that the structural changes that are observed in "Mag-cos" mode are more notable (fig. 15 a - d).

The rapid decrease of the intergranular boundaries contrast is observed. At starting sintering stages (relative density of 0.92, fig. 15, a) the boundaries between grains look like light lines. Such "brightening" of the boundaries is connected with the AFM apparatus peculiarities at the analysis surface with large slope. Large height difference on the grain boundaries allows to conclude that the fracture of the 0.92 dense ceramics takes place along the grain boundaries.

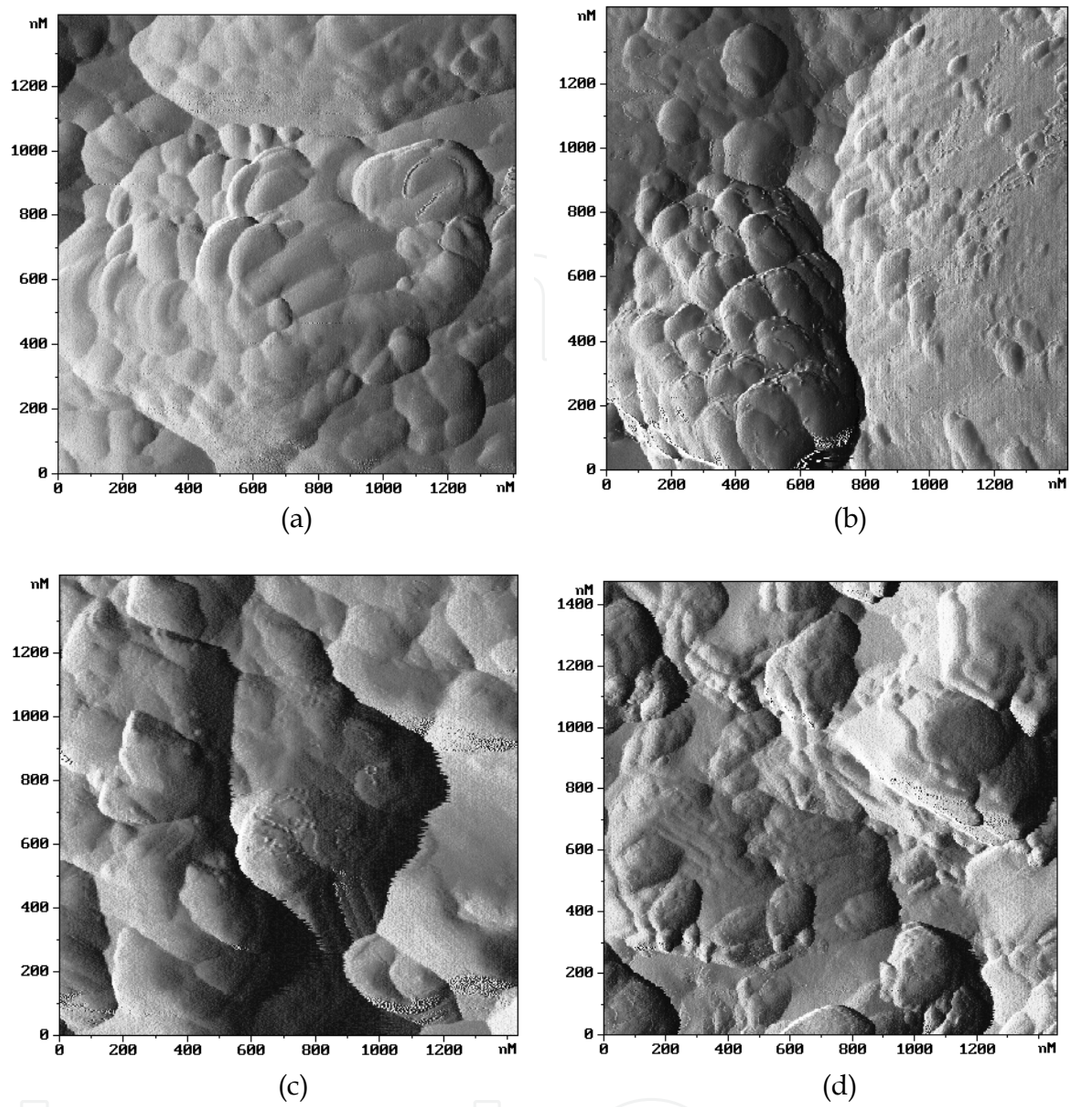

Fig. 14. Fracture AFM images in "height" mode of Al_2O_3 + t-YSZ ceramics at relative densities of 0.92: (a) – A93, (b) – AZ10 and 0.97: (c) – A93, (d) - A85.

The images of the 0.97 dense ceramics taken at "Mag-cos" mode (fig. 15, b) differ a lot: large white and small dark regions are distributed randomly. As the volume fraction of $\alpha-Al_2O_3$ phase is larger than t-YSZ fraction in A93, A85 and AZ10 ceramics, one can assume that light regions are the large corundum blocks and dark regions are the insertions of zirconia. It should be pointed out that "Mag-cos" images of A93 ceramics sintered from laser powder (fig. 15, b) are the same as for A85 ceramics sintered from the mechanical powder mixtures (fig. 15, c).

In case of AZ10 ceramics (fig. 14 d and 15 d) the non-uniformity of the block's shape and size should be pointed out. Probably such huge difference from A85 (having almost the same composition and prepared by the same route) is connected with the non-uniform distribution of ZrO_2 dopant in the initial AZ10 powder.

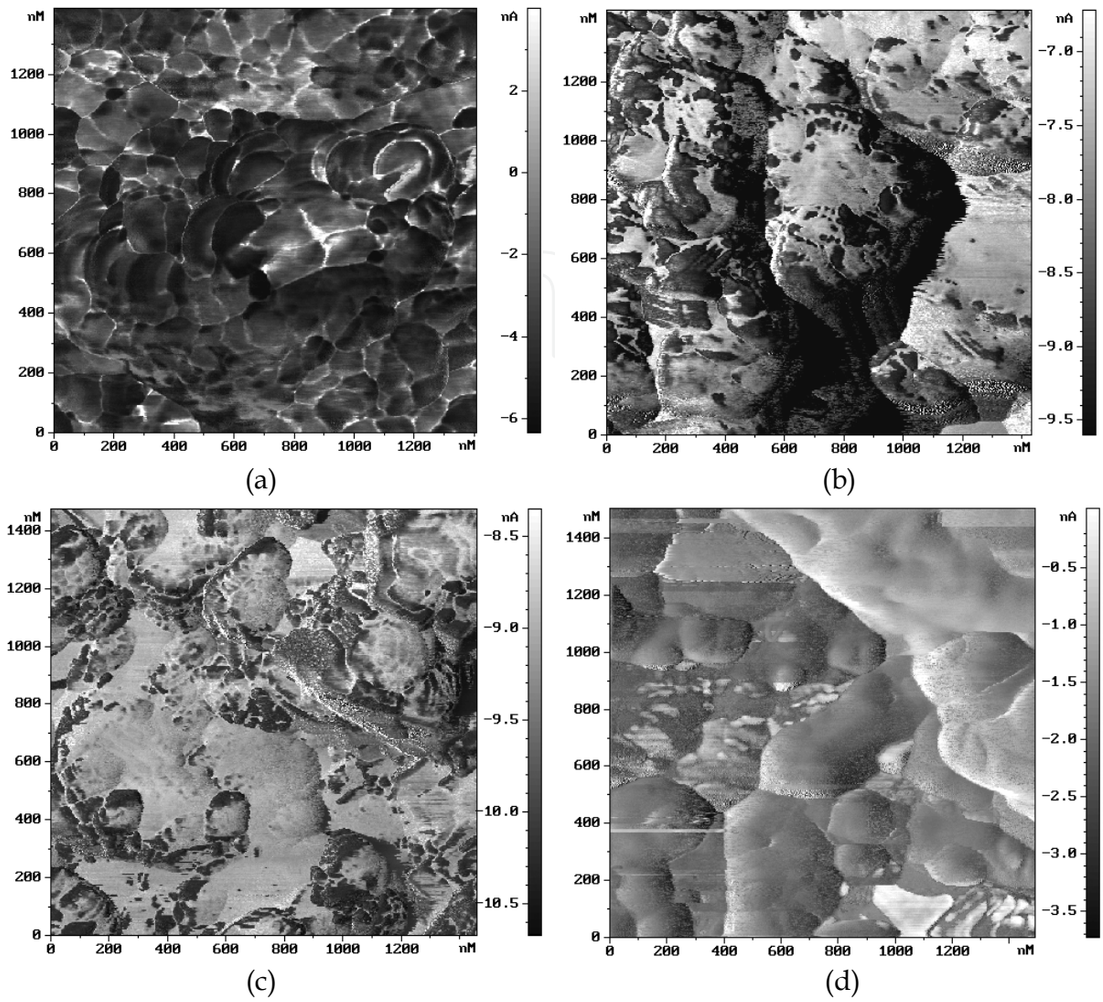

Fig. 15. Al_2O_3 + t-YSZ ceramic fracture AFM images in "Mag-Cos" mode (a) – A93 (relative density 0.92), (b) – A93 (c) – A85, (d) - AZ10 (relative density 0.97).

AFM images of A40 ceramics fracture in "Mag-cos" mode (fig. 16) show the equidimensional dark and light regions, distributed over the image area more uniformly compared to the fracture images of other ceramics (fig. 15, b and c). Thus in this ceramics the oxide grains are mixed quite well.

It looks interesting to compare the grain size obtained from AFM images analysis and from X-ray data (table 4). The X-ray grain size in A85 and A93 ceramics is larger than the confirmative range of the method. The X-ray analysis showed that in A40 and A45 ceramics the X-ray crystallite size is small being twice as small as obtained from AFM data. Moreover, according to AFM data the grain size in the ceramics sintered from nanopowders obtained by different methods doesn't differ and is 280±10 nm. The difference in the values is logical as AFM shows the size of the "blocks" which can consist of a large number of crystals with small X-ray crystallite size. The cantilever tip has a radius of about 5 - 10 nm. Therefore if the boundary width between crystals is smaller than this value it's not registered by this method.

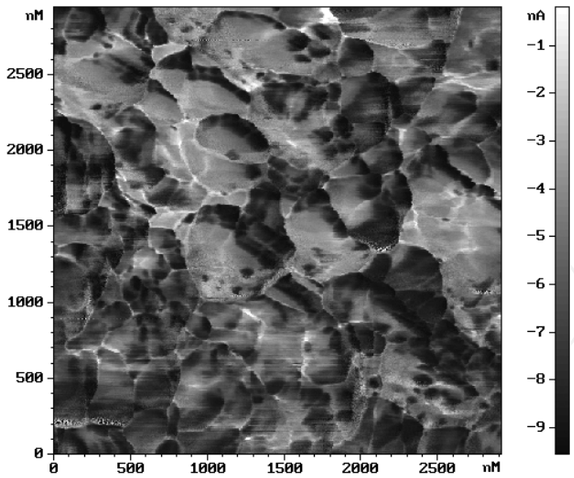

Fig. 16. A40 ceramic fracture AFM image in "Mag-Cos" mode, relative density 0.99.

4.4 Hardness and fracture toughness of submicron alumina-based ceramics

For the fabrication of the full dense ceramics for each powder type the corresponding temperature and dwell time were picked for at least 65% green bodies. The main characteristics of the ceramic samples are shown in table 4. All samples contained stable modifications. In the ceramics sintered from composite LE nanopowders (A45 and A93) up to 3% of monoclinic zirconia was found.

The microhardness of all ceramic samples was in 17-21 GPa range. The best hardness of 21 GPa had AM1 (MgO doped alumina) ceramics. This value is comparable to the hardness of monocrystall alumina – leucosapphire 20.9 GPa. High ceramics properties (table 4) prove the assumption that particle aggregates of the powders obtained by MPC and LE methods are weak and don't influence the compaction process with the following sintering.

The microhardness of the ceramics containing t-YSZ depends on its amount and increases from 17 up to 20 GPa with the decrease of t-YSZ amount from 60 down to 7 wt.%. It should be noted that for A93 ceramics sintering the highest temperature of 1490°C was used. At that its relative density being 0.961 was the lowest one in the row of the ceramics studied.

The microhardness of the ceramic samples with large fraction of YSZ (A40 and A45) being 17 GPa is close to the values of the individual 2.8YSZ. This is defined probably by the presence of YSZ matrix where the corundum grains are distributed. Fracture toughness of the ceramics containing t-YSZ was in 5 - 6 MPa·$m^{½}$ range.

Wear resistance is the most important integral property of the material, showing the package of its mechanical properties. The comparative analysis of the wear resistance of 3 types of ceramics (ZrO_2, MgO or TiO_2 doped alumina) showed that the specific wear resistance correlates with the microsturcture characteristics and with the hardness of the ceramics. The samples with finer structure and higher hardness have better were resistance. Thus in order to achieve high wear resistance of the ceramics it is necessary to decrease grain size at high density.

powder type	dopa-nt	t_S, °C	τ_S, min	ρ, g/cm³	H_V, GPa	K_{1C}, MPa·m½	d_X α-Al_2O_3 nm	d_X ZrO_2 nm	d_{ACM}, nm	ε g/(kW·h)	Ra nm	phase content
Al_2O3	-	1410	2	0.941	21		> 200	-	-			α-Al_2O_3
AM1	MgO	1410	5	0.976	14		180	-	-			96 - α-Al_2O_3 + 4 - $MgAl_2O_4$
		1450	6	0.969	21	4	180	-	200-300	0.04	29	
		1450	30	0.973	20	4	> 200	-	300-500	0.06	43	
AT1	TiO_2	1450	6	0.961	17	3	> 200	-	200-800	0.13	130	99 - α-Al_2O_3 +
		1450	60	0.972	17	4	> 200	-	300-1000	0.14	180	1 - R-TiO_2
AZ10	ZrO_2	1450	6	0.920	13	4	150	-	200-300			90 - α-Al_2O_3
		1450	60	0.977	19	5	> 200	70	300-600	0.07	92	7,5 - t-ZrO_2 2,5 - m-ZrO_2
A45	1,6YSZ	1410	120	0,982	17	5	> 200	80	-			45α + 52t + 3m
A40	2.8YSZ	1410	15	0.997	17	5	140	70	300-400			40α + 60 t
A93	1.6YSZ	1490	0	0.961	20	5	> 200	55	300-400			93α + 7t+m
A85	2.8YSZ	1450	60	0.980	18	6	> 200	70	300-400			85α + 15t

t_S i τ_S - sintering temperature and dwell time, ρ - density, H_V - microhardness, K_{1c} - fracture toughness, d_x- average X-ray crystallite size defined by the X-ray analysis, d_{AFM} – average grain size according AFM data, ε - specific wear; R_a - roughness of attacking surface; R – rutile, t and m – tetragonal and monoclinic forms of YSZ.

Table 4. The characteristics of the ceramics based on Al_2O_3.

The comparison of the wear resistance of AM1 ceramics with commercial XC22 corundum ceramics showed more than 3 times higher resistance of AM1 ceramics. This can substantially increase the life time of the devices without fixing.

The investigation data of the external surface of the ceramic samples after the wear testing via the optical interferential microscope with 2000x magnification logically complement and correlate with the information about the internal microstructure and the resistance of the ceramics to the wear action. The main peculiarities of the sample's surface structure are demonstrated by the projected images of the relief (fig. 3.18). The standard roughness of the attacking surface of all samples is shown in table 4. The attacking surface of the most wear resistant AM1 ceramics has the most homogenous surface structure at the absence of macro defects and the lowest roughness R_a = 29 nm (fig. 17, a). For AM1 ceramics with prolonged sintering dwell time the carryover of the material during wear characterizes with the round-shaped cavities up to 5 microns in size and up to 0.3 microns deep (fig. 17, b) at low average roughness. In case of AT1 ceramics, sintered for 6 minutes, the carryover tracks have 10 microns jagged shape (fig. 17, c). Upon wearing of AT1 ceramics with prolonged sintering dwell time (60 minutes) (fig. 17, d) the increase of fracture non-uniformity and grain size of the

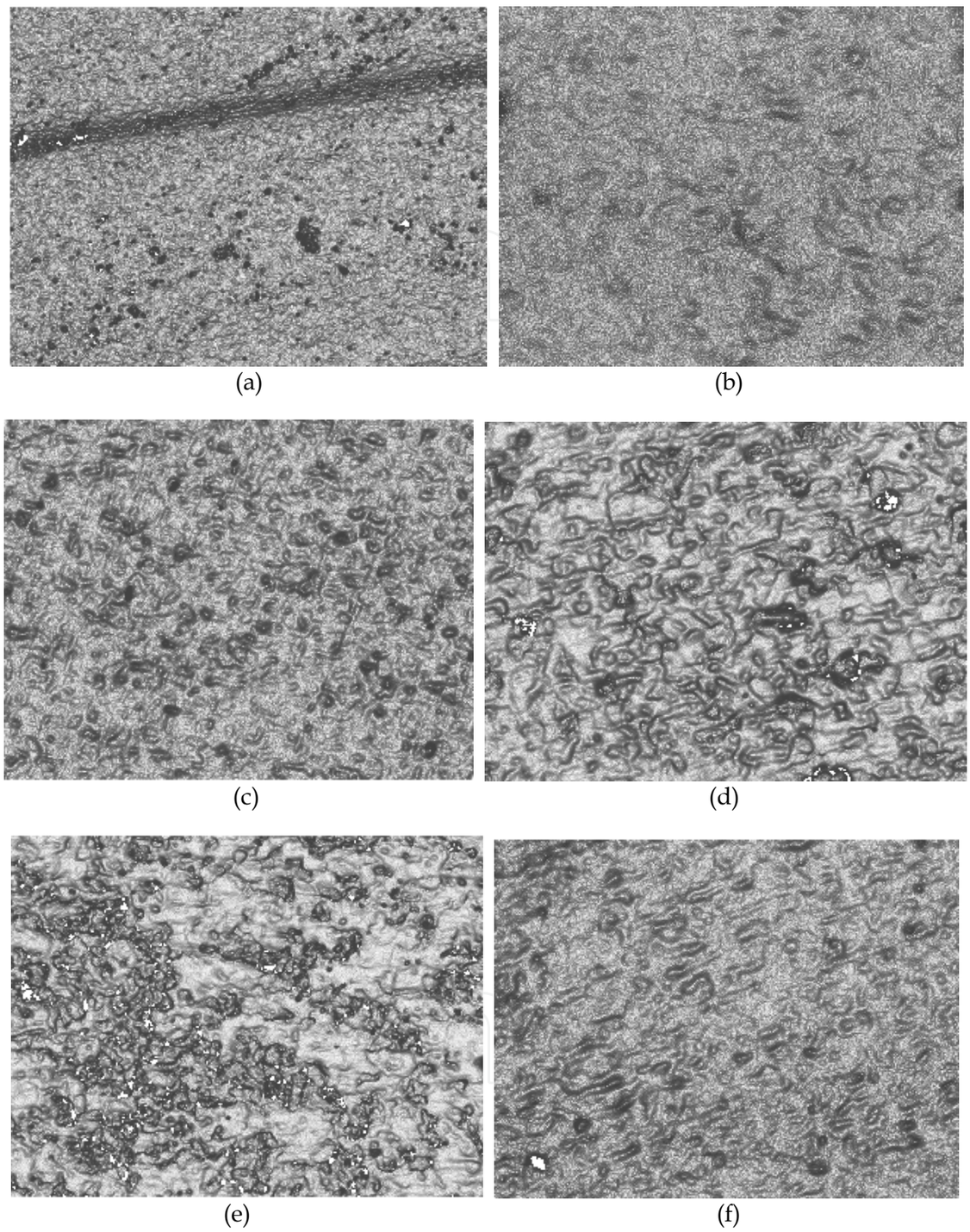

Fig. 17. The characteristic images of the working surfaces of the submicron ceramics after the wear test: the attack surface (2000x): (a) - AM1 (τs = 6 min), (b) - AM1 (τs = 30 min), (c) AT1 (τs = 6 min), (d) - AT1 (τs = 60 min), (e) - AZ10 (τs = 60 min) ; (f) sliding surface (1000x) AM1 (τs = 6 min. Image area at 2000x - 70x50 microns, at 1000x 40x110 microns.

erosion cavities up to 20 microns at the depth of 1.5 microns was observed. The damage dimensions of the AZ10 ceramics surface is much less and its low roughness R_a = 92 nm (fig. 17, d) correlates with high wear resistance comparing to AT1 ceramics. Though two types of ceramics doped with TiO_2 and ZrO_2 had sufficient difference in wear factor (ε, table 4) they are characterized with notable relief trend corresponding to the direction of the abrasive flow.

The wear of the working surface of the sample (in addition to the abovementioned peculiarities) is characterized by the 2-3 times elevated roughness and gutter formation, oriented along the moving direction. In particular fig. 17 illustrates this peculiarity for AM1 (dwell time - 6 minutes) ceramics with the characteristic gutter width of 15 microns and depth of 1.5 microns correspondingly.

The abovementioned data show that among the types of ceramics with α-Al_2O_3 matrix the composition containing homogeneously dispersed $MgAl_2O_4$ second phase is the best one. At that the homogeneity of MgO dopant was provided during the nanopowder synthesis via EEW of Al-Mg alloy. During sintering the aluminum-magnesium spinel second phase segregates and covers the surface of the formed crystallites α-Al_2O_3 (fig. 10) uniformly. This inhibits the mass movement processes and eliminates the grain growth of α-Al_2O_3 crystals effectively. Being anisotropic, corundum creates the inhomogenety of properties (hardness and microstructure stress) in polycrystal body. The decrease of the grain size leads to the decrease of the effect of the properties change moving from one grain to another. This leads to the increase of wear resistance upon the decrease of structure scale.

MgO doped alumina ceramics showed the best characteristics. In this ceramics the homogeneous distribution of the dopant was provided by the nanopowder synthesis method.

Small grain size was obtained due to high starting density of the green bodies. The use of MPC of weakly aggregated nanopowders made it possible. At that the larger contact area of the particles and high homogeneity level of the compact are reached. At elevated level of defects of intergranular boundaries and large amount of crystallization centers of α-Al_2O_3 this creates height starting position for the polymorph transition and for the shrinkage. Also it allows to conduct sintering at relatively low temperatures in 1400-1450°C range.

5. Conclusions

1. The usage of weakly aggregated nanopowders of unstable alumina phases, compacted by MPC method up to high density more than 0.65 (relative to theoretical one) allows obtaining dense ceramics with submicron structure at relatively low sintering temperatures in the 1400-1450°C range and up to 30 minutes dwell time.
2. The wear resistance of the ceramics correlates with the structural scale, density and dopant nature. In the row of the TiO_2 – ZrO_2 – MgO additives the wear characteristics of alumina increases sufficiently. The MgO doped ceramics, which is characterized with the smallest grain size of around 300 nm upon high density and hardness appears to have the best parameters.
3. The sintering at reduced down to 1450°C temperatures allowed to obtain the alumina-based ceramics which is 2.5-3 times more resistant to abrasive-erosive wear comparing with the best industrial ceramics with the same composition. Such ceramics combine high density, 0.97, small grain size of the alumina (<300 nm) and $MgAl_2O_4$ spinel (20 nm), high

hardness (20-21 GPa) and fracture toughness (4 MPa·$m^{0.5}$). The ceramics is fabricated from metastable (γ and δ - phases) alumina nanopowder with the soluted magnesia in it.

4. It was found that the microhardness of the nanosized alumina / tetragonal zirconia (T-YSZ) composite ceramics depends from the T-YSZ amount and increases from 17 to 20 GPa with the decrease of its amount from 60 down to 7 wt.%. The fracture toughness of the samples is around 5-6 MPa·$m^{0.5}$. At that the best elimination of the crystallites growth of alumina (140 nm) was observed for the composite ceramics with the equal amount of α-Al_2O_3 and T-YSZ phases and sintered at 1410°C up to the relative density of 0.997.

6. References

Bragin V.B., Ivanov V.V., Ivanova O.F., Ivin S.Yu., Kotov Yu.A., Kaygorodov A.S., Kiriakov S.I., Medvedev A.I., Murzakaev A.M., Postnikov V.S., Neshkov P.F., Khrustov V.R. & Shtoltz A.K. (2004). Wear resistance of a fine structured ceramics based on $A1_2O_3$ doped with magnesium, titanium or zirconium. *Perspectivnye materialy,* No.6. - pp. 48 - 56. (in russian)

Chen D-J. & Mayo M.J. (1993). Densification and grain growth of ultrafine 3 mol % Y_2O_3-ZrO_2 ceramics. Nanostruct. Materials, Vol. 2, – pp. 469 - 478.

Freim J., Mckittrick J., Katz J. & Sickafus K. (1994). Microwave Sintering of Nanocrystalline γ- $A1_2O_3$. Nanostructured Materials, Vol. 4, No 4, pp. 371 - 385.

Graham R.A. & Thadhani N.N. (1993). Solid State Reactivity of Shock-Processed Solids. In Shock Waves in Materials Science, Sawaoka A.B., pp. 35 - 99, Springer-Verlag.

Hahn H. & Averback R.S. (1992). High Temperature Mechanical Properties of Nanostructured Ceramics. Nanostruct. Materials, Vol.1, - pp. 95 - 100.

Ivanov V.V., Kotov Yu.A., Samatov O.H., Boehme R., Karov H.U. & Schumacher G. (1995). Synthesis and dynamic compaction of ceramic nano powders by techniques based on electric pulsed power. Nanostruct. Materials. Vol. 6, No 1 - 4, pp. 287 - 290.

Ivanov V.V., Paranin S.N., Vikhrev A.N. & Nozdrin A.A. (1997). The efficiency of the dynamic method of sealing nanosized powders, Materialovedenie, No 5, pp. 49 – 55 (in Russian)

Ivanov V., Paranin S., Khrustov V. & Medvedev A. 1999. Fabrication of articles of nanostructured ceramics based on Al2O3 and ZrO2 by pulsed magnetic compaction and sintering, Proc. of 9th World Ceramic Congress Cimtec - Ceramics: Getting into the 2000's, - Florence, Italy,. - Part C. - pp. 441 - 448.

Lange F.F. (1984). Sinterability of Agglomerated Powders, Journal of Amer. Cer. Soc, Vol. 67, No 2, – pp. 83 – 89.

Kotov Yu.A., Osipov V.V., Ivanov M.G., Samatov O.M., Platonov V.V., Azarkevich E.I., Murzakaev A.M. & Medvedev A.I. (2002). Properties of oxide nanopowders prepared by target evaporation with pulse-periodic CO_2 laser. Technical Physics, Vol. 47, No. 11. pp. 1420-1426.

Kotov Yu.A. (2003). Electric explosion of wires as a method for preparation of nanopowders. Journal of nanoparticle research. Vol.4, pp. 539 - 550

Smothers W.J. & Reynolds H.J. (1954). Sintering and grain growth of alumina. Journal of. Amer. Cer. Soc, V. 37. - No 12, pp. 588 - 595.

Srdic´ V.V., Rakic´ S & Cvejic´ Z. (2008). Aluminum doped zirconia nanopowders: Wet-chemical synthesis and structural analysis by Rietveld refinement. Materials Research Bulletin, Vol.43, - pp. 2727 – 2735

Vassen R. & Stoever D. (1992). Compaction Mechanisms of Ultrafine SiC Powders. Powder Technology, Vol.72, pp.223 - 226.

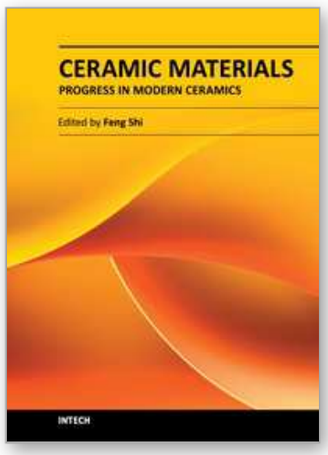

Ceramic Materials - Progress in Modern Ceramics

Edited by Prof. Feng Shi

ISBN 978-953-51-0476-6
Hard cover, 228 pages
Publisher InTech
Published online 05, April, 2012
Published in print edition April, 2012

This text covers ceramic materials from the fundamentals to industrial applications. This includes their impact on the modern technologies, including nano-ceramic, ceramic matrix composites, nanostructured ceramic membranes, porous ceramics, and the sintering theory model of modern ceramics.

How to reference

In order to correctly reference this scholarly work, feel free to copy and paste the following:

V. V. Ivanov, A. S. Kaygorodov, V. R. Khrustov and S. N. Paranin (2012). Fine Grained Alumina-Based Ceramics Produced Using Magnetic Pulsed Compaction, Ceramic Materials - Progress in Modern Ceramics, Prof. Feng Shi (Ed.), ISBN: 978-953-51-0476-6, InTech, Available from: http://www.intechopen.com/books/ceramic-materials-progress-in-modern-ceramics/fine-grained-alumina-based-ceramics-produced-using-magnetic-pulsed-compacting

INTECH
open science | open minds

InTech Europe
University Campus STeP Ri
Slavka Krautzeka 83/A
51000 Rijeka, Croatia
Phone: +385 (51) 770 447
Fax: +385 (51) 686 166
www.intechopen.com

InTech China
Unit 405, Office Block, Hotel Equatorial Shanghai
No.65, Yan An Road (West), Shanghai, 200040, China
中国上海市延安西路65号上海国际贵都大饭店办公楼405单元
Phone: +86-21-62489820
Fax: +86-21-62489821

IntechOpen